



Three-dimensional simulation of tsunami generation and propagation: Application to intraplate events

Tatsuhiko Saito^{1,2} and Takashi Furumura^{1,2}

Received 25 November 2007; revised 2 December 2008; accepted 12 December 2008; published 17 February 2009.

[1] A parallel finite difference numerical simulation program based on the Navier-Stokes (NS) equations is developed for simulating 3-D tsunami generation and propagation. We can simulate tsunami propagation over more than 1000 km using this program, although such tsunami propagation over long distances has usually been conducted on the basis of on 2-D simulations. Some 2-D simulations have assumed that the initial tsunami distribution is identical to the sea bottom deformation caused by the earthquake. The 3-D simulations, however, indicate that this assumption is inappropriate when the source width $2a_x$ is less than 10 times the sea depth h ($2a_x < 10h$) for a source process time of 20 s. Dispersion of tsunami appears when the source is of small size, and the dispersion is more apparent in a direction perpendicular to the fault strike. We also conduct tsunami simulations for two intraplate events: the 2004 off-Kii Peninsula (M 7.4) and the 2007 off-Kuril Islands (M 8.1) events. The 3-D tsunami simulation has successfully simulated the offshore tsunami, and we obtained good agreement between the observations and the calculations for both events. In particular, for the 2004 off-Kii Peninsula event, although the 2-D linear long-wave theory cannot simulate important characteristics in the record such as the arrival time of the peak amplitude and the dispersive tsunami, the 3-D NS simulation is well able to model those characteristics.

Citation: Saito, T., and T. Furumura (2009), Three-dimensional simulation of tsunami generation and propagation: Application to intraplate events, *J. Geophys. Res.*, *114*, B02307, doi:10.1029/2007JB005523.

1. Introduction

[2] Tsunami simulations have been conducted mostly in 2-D space on the basis of the long-wave approximation, instead of solving 3-D Navier-Stokes (NS) equations. Simulations based on the 2-D linear long-wave (LLW) equations are cost effective and widely used for tsunami propagation, especially for offshore tsunami [e.g., *Fujii and Satake*, 2007]. They are often employed to derive tsunami Green functions for the estimation of slip distribution along seismic faults or of an initial tsunami distribution [e.g., *Satake*, 1989; *Baba et al.*, 2006]. They are also used in tsunami hazard assessments for past and expected future large earthquakes [e.g., *Geist*, 2002]. Dispersive long-wave equations such as Boussinesq equations are an attractive alternative that include higher-order terms to simulate dispersive tsunami in 2-D space [e.g., *Yoon*, 2002; *Shigihara and Fujima*, 2007]. Considering tsunami in very shallow sea relative to their height, such as tsunamis that are approaching coasts and entering bays, nonlinear effects should be taken into consideration [e.g., *Heinrich et al.*, 2001].

[3] Because 2-D simulations employ long-wave approximations and so do not allow calculation of the vertical flow, the tsunami generation process due to the sea bottom uplifting is not usually calculated, but given as a source in the 2-D simulations. There are some methods for implementing the tsunami source. Numerous 2-D tsunami simulations assume that the initial tsunami distribution is identical to the sea bottom deformation caused by the earthquake [e.g., *Piatanesi and Lorito*, 2007]. Alternatively, some papers take finite duration of the sea bottom deformation into account by adding the sea bottom deformation within a time step to the tsunami height distribution at each time step in the simulation [e.g., *Fujii and Satake*, 2007]. Those methods may be valid for many tsunamigenic earthquakes that occur along the subducting plate and cause deformation of the sea bottom over a large area. However, a small sea bottom deformation area would not result in as great an uplift of the sea surface as would occur for the sea bottom. This is indicated by the tsunami generation studies supposing potential flow and using the linear approximation [e.g., *Kajiura*, 1963; *Ward*, 2001]. We referred to those theories as the linear approximation theory hereinafter, in this manuscript. The linear approximation theory can derive the relation between the sea bottom deformation and the excited tsunami under the assumption that the sea depth is constant. Some 2-D tsunami simulation studies employ the linear approximation theory for the estimation of the initial tsunami distribution [e.g., *Tanioka and Seno*, 2001].

¹Earthquake Research Institute, University of Tokyo, Tokyo, Japan.

²Core Research for Evolutional Science and Technology, Japan Science and Technology Agency, Kawaguchi, Japan.

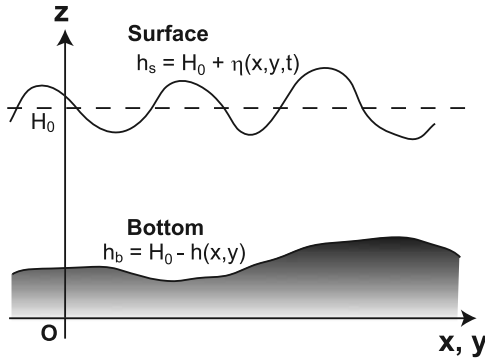


Figure 1. Model geometry of the Cartesian coordinates (x, y, z) used in the present study.

[4] Without using the above assumption or the linear approximation theory, the 3-D tsunami simulation can simulate the tsunami generation process caused by the sea bottom deformation. Furthermore, the 3-D simulation naturally includes a dispersion effect which is neglected in the 2-D LLW equations. Recent studies have indicated that 3-D tsunami simulation based on the finite difference method (FDM) or boundary element method (BEM) is a promising tool for tsunami generation and propagation simulation [e.g., *Ohmachi et al.*, 2001; *Mader*, 2004]. The scale of the simulations at present, however, is limited to relatively small distances (50~400 km) [e.g., *Matsumoto and Mikada*, 2005; *Kervella et al.*, 2007]. In order to apply the 3-D simulation to observed records, it is important to develop a suitable simulation code for distant tsunami propagation using parallel computers.

[5] This study develops a parallel simulation program for solving the 3-D NS equations on a large scale in order to simulate tsunami generation and propagation over realistic bathymetry. In the present manuscript, we first give a brief explanation of the NS equations and an efficient numerical technique for solving the equations which was originally proposed by *Hirt et al.* [1975]. A parallel algorithm and the efficiency of the simulation using a large number of processors are also demonstrated. We then use the tsunami simulations to investigate the tsunami excitation and propagation properties for different models with various source sizes and sea depths. Finally, 3-D tsunami simulations are conducted for two recent intraplate events which occurred in and around Japan, the 2004 off-Kii Peninsula (M 7.4) and the 2007 off-Kuril Islands (M 8.1) earthquakes.

2. Governing Equations for Tsunamis

2.1. Navier-Stokes Equations

[6] The motion of a fluid is described by the following 3-D NS equations, where we take the z axis in the vertical direction and the x and y axes in horizontal space in Cartesian coordinates (Figure 1):

$$\begin{cases} \frac{\partial u}{\partial t} + u \frac{\partial u}{\partial x} + v \frac{\partial u}{\partial y} + w \frac{\partial u}{\partial z} = -\frac{\partial}{\partial x} \left(\frac{p}{\rho_0} \right) + \nu \nabla^2 u \\ \frac{\partial v}{\partial t} + u \frac{\partial v}{\partial x} + v \frac{\partial v}{\partial y} + w \frac{\partial v}{\partial z} = -\frac{\partial}{\partial y} \left(\frac{p}{\rho_0} \right) + \nu \nabla^2 v \\ \frac{\partial w}{\partial t} + u \frac{\partial w}{\partial x} + v \frac{\partial w}{\partial y} + w \frac{\partial w}{\partial z} = -\frac{\partial}{\partial z} \left(\frac{p}{\rho_0} \right) + \nu \nabla^2 w - g \end{cases} \quad (1)$$

where u , v , and w are velocity components along the x , y , and z axes, respectively, p is pressure, g is acceleration due to gravity, ρ_0 is the density, and ν is the kinematic viscosity coefficient for seawater [e.g., *Snider*, 2001]. The viscosity of seawater is characterized by a very small value of $\nu = 10^{-6} \text{ m}^2 \text{ s}^{-1}$. We may consider that offshore tsunami motion is nonturbulent [e.g., *Stoneley*, 1964].

[7] Assuming incompressible fluid flow, the continuity equation is given by

$$\frac{\partial u}{\partial x} + \frac{\partial v}{\partial y} + \frac{\partial w}{\partial z} = 0. \quad (2)$$

[8] When we take a free surface at rest as $z = H_0$, the bottom is given by $z = h_b = H_0 - h(x, y)$ where $h(x, y)$ is the sea depth. The free surface is given by $z = h_s(x, y, t) = H_0 + \eta(x, y, t)$, where $\eta(x, y, t)$ is the fluctuation of the surface at time t . We may consider $\eta(x, y, t)$ as the tsunami. The kinematic boundary condition at the sea surface is given by

$$\frac{\partial \eta}{\partial t} + u \frac{\partial \eta}{\partial x} + v \frac{\partial \eta}{\partial y} = w \text{ for } z = h_s(x, y, t). \quad (3)$$

[9] This boundary condition cannot take account of tsunami breaking or inundation near a sloping shore (the runup problem), which are therefore excluded from the subject of this study. The above equations govern the behavior of offshore tsunamis.

2.2. FDM Simulation of Navier-Stokes Equations

[10] We use the technique developed by *Hirt et al.* [1975] to solve equations (1), (2), and (3). The NS equations are solved numerically using the FDM with a staggered-grid model. The FDM mesh for the staggered grid is composed of cubic cells in Cartesian coordinates (Figure 2a). The velocities and pressure components are distributed in each cell with a half-grid dislocation from each other as shown in Figure 2b.

[11] The simulation starts with a hydrostatic pressure field; the pressure increases linearly with increasing depth from the surface and is set to be zero above the surface of the sea:

$$p(z) = \begin{cases} 0 & \text{for } z \geq H_0 \\ g(H_0 - z) & \text{for } z < H_0. \end{cases} \quad (4)$$

[12] The deformation of the bottom is directly introduced into the simulation through the water flow at the cell at the bottom. Suppose that the bottom is rising linearly with constant velocity and with final vertical displacement distribution at the bottom after the source process time t_s being given by $d(x, y)$; the corresponding boundary condition at the bottom is then given by

$$w(x, y, h_b(x, y)) = \begin{cases} d(x, y)/t_s & \text{for } 0 < t \leq t_s \\ 0 & \text{for } t > t_s. \end{cases} \quad (5)$$

[13] The vertical flow caused by the bottom deformation results in elevation of the surface. The elevation, or the height distribution at the surface, is propagated as a tsunami.

[14] The height distribution at the surface $\eta(x, y, t)$ depends on the velocity field of the water flow (equation (3)). Using the pressure and the velocity field at the present time t ,

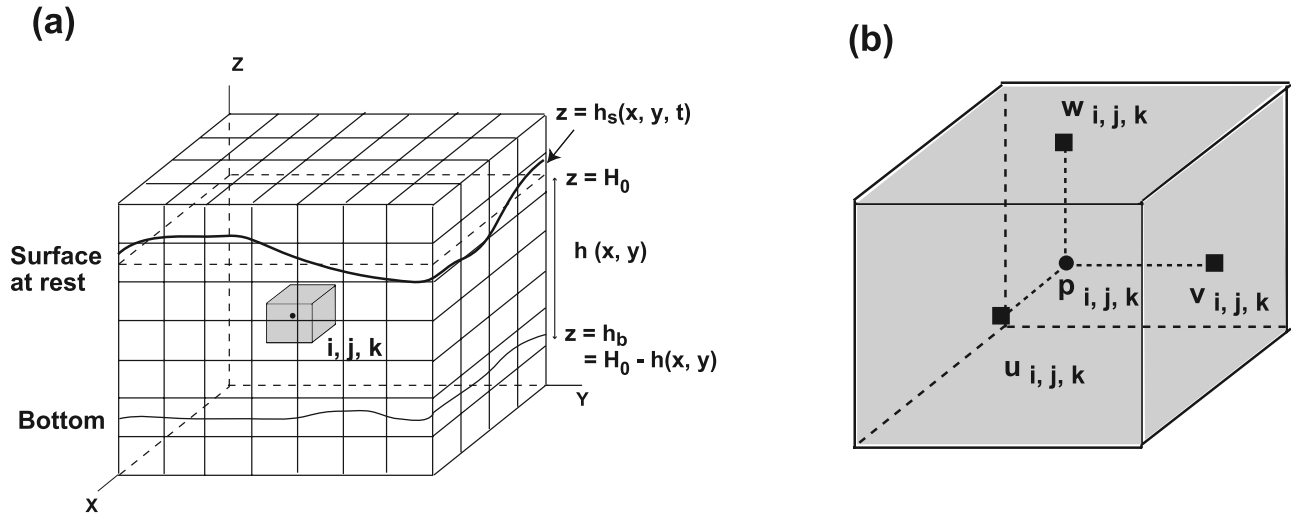


Figure 2. (a) The staggered-grid finite difference mesh used in the 3-D tsunami simulation. The mesh is composed of cubic cells. The surface at rest is located at $z = H_0$, and the bottom is located at $z = h_b(x, y) = H_0 - h(x, y)$. The free surface to be calculated is given by $z = h_s(x, y, t)$. (b) Arrangement of variables in the cell (i, j, k) .

the new velocity field at the next time step $t + \Delta t$ is numerically calculated from equation (1) by means of the FDM. The nonlinear terms in equation (1) often cause numerical instability problems. Thus, a mixture of the up-stream and central finite difference schemes are employed in the simulation to increase stability [Hirt *et al.*, 1975]. The resultant velocity field from equation (1) will not, in general, satisfy the continuity equation (2) and so the divergence D for each cell,

$$D = \frac{1}{\Delta x} (u_{i,j,k} - u_{i-1,j,k}) + \frac{1}{\Delta y} (v_{i,j,k} - v_{i,j,k-1}) + \frac{1}{\Delta z} (w_{i,j,k} - w_{i,j,k-1}), \quad (6)$$

does not necessarily vanish. In order to satisfy the incompressibility constraint of equation (2) in each cell, we must adjust the cell pressures and the adjacent velocity field at each time step. The pressure change δp required to make D equal to zero is

$$\delta p = -\frac{D\Delta x^2}{4\Delta t}, \quad (7)$$

and the velocity corrections for adjacent grid points are as follows:

$$\begin{aligned} u_{i,j,k} &\rightarrow u_{i,j,k} + \frac{\Delta t \delta p}{\Delta x}, \\ u_{i-1,j,k} &\rightarrow u_{i-1,j,k} - \frac{\Delta t \delta p}{\Delta x}, \\ v_{i,j,k} &\rightarrow v_{i,j,k} + \frac{\Delta t \delta p}{\Delta y}, \\ v_{i,j-1,k} &\rightarrow v_{i,j-1,k} - \frac{\Delta t \delta p}{\Delta y}, \\ w_{i,j,k} &\rightarrow w_{i,j,k} + \frac{\Delta t \delta p}{\Delta z}, \\ w_{i,j,k-1} &\rightarrow w_{i,j,k-1} - \frac{\Delta t \delta p}{\Delta z}. \end{aligned} \quad (8)$$

[15] This adjustment is made for all cells in the simulation model, iteratively, until the divergence of all cells converges almost to zero. After convergence of D reaches an acceptable level (e.g., $D < 10^{-7}$), the free surface $z = h_s(x, y, t)$ is calculated according to equation (3).

[16] The time step Δt of the FDM simulation is chosen to satisfy the following condition: $\Delta t < \min \{ \Delta x/|u|, \Delta y/|v|, \Delta z/|w| \}$. A nonslip boundary condition at the bottom is introduced by setting $u = 0, v = 0, w = 0$, except during the source process time ($t < t_s$). A sponge buffer zone [Cerjan *et al.*, 1985] is created at the 20 grid points surrounding the simulation model in order to reduce the reflection of tsunami at physical boundaries.

2.3. Parallel Computation of Solutions to the Navier-Stokes Equations

[17] We develop a parallel program for offshore tsunamis that are excited by the bottom deformation and that propagate over 1000 km. The parallel algorithm is based on a traditional domain partitioning procedure, where the 3-D model is partitioned horizontally into many subregions with one-cell overlapping with neighboring subregions (Figure 3). Each processor calculates the velocity and pressure fields at each grid point in the assigned subregion, and a message-passing interface (MPI) is used for exchanging data between neighboring subregions at each time step.

[18] The parallel tsunami code has been implemented on a cluster of PCs consisting of 16 AMD Opteron processors, (1.4 GHz CPU clock speed), connected over a fast Infini-band computer network (communication speed of 1 Gb s⁻¹). Figure 4 illustrates the results of parallel computing in terms of faster execution of the computation using a large number of CPUs. A fairly good improvement in speed and thus a reduction in elapsed time for the 3-D tsunami simulation is found with increasing processor numbers from 2, 4, up to 8 for a smaller simulation model of $512 \times 512 \times 204$ grid points, which takes computer memory of about 3 Gb when using double-precision arithmetic. However,

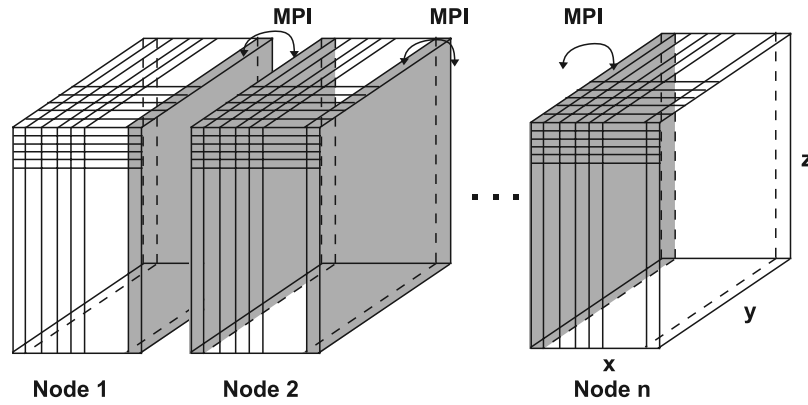


Figure 3. The parallel FDM model for 3-D tsunami simulations. The 3-D model is partitioned horizontally into many subregions, and a message-passing interface (MPI) is used for exchanging data between neighbor processors in the overlapping (shaded) area.

parallel computing using more processors (16) does not result in good performance with the present simulation model. This is because of the overhead of the MPI communication between large numbers of processors relative to the total computation time of the NS equations for the divided model.

[19] On the other hand, good parallel performance with increasing computational speed using a large number (16) processors is confirmed for a large simulation model of $512 \times 1024 \times 204$, $512 \times 2048 \times 204$, and $512 \times 4096 \times 204$ grid points, which required computer memory of about 6 GB, 12 GB, and 24 GB, respectively.

[20] The tests demonstrate the effectiveness of the parallel FDM simulation for solving 3-D NS equations in large-scale model using large number of processors. Care is needed to match the appropriate number of processors to the scale of the simulation model in order to ensure good parallel performance.

2.4. The 2-D Tsunami Equations

[21] For conventional tsunami simulations, 2-D tsunami equations have often been employed. The equations can be derived from the NS equations, the continuity equation, and the kinematic boundary condition at the surface, integrating the water flow along the vertical (z) direction from the sea bottom to the sea surface, assuming that the tsunami wavelength is much longer than the sea depth, and that the surface fluctuation η is much smaller than the sea depth h [e.g., *Stoker*, 1958; *Goto*, 1984]. The 2-D linear dispersive (DSP) equations in weak sea bottom fluctuation are obtained from the NS equations as

$$\begin{aligned} \frac{\partial M}{\partial t} + gh \frac{\partial \eta}{\partial x} &= \frac{1}{3} h^2 \frac{\partial^2}{\partial x \partial t} \left(\frac{\partial M}{\partial x} + \frac{\partial N}{\partial y} \right), \\ \frac{\partial N}{\partial t} + gh \frac{\partial \eta}{\partial y} &= \frac{1}{3} h^2 \frac{\partial^2}{\partial y \partial t} \left(\frac{\partial M}{\partial x} + \frac{\partial N}{\partial y} \right) \end{aligned} \quad (9)$$

and the continuity equation is

$$\frac{\partial(\eta + h)}{\partial t} = -\frac{\partial M}{\partial x} - \frac{\partial N}{\partial y}, \quad (10)$$

where

$$M = \int_{H_0-h}^{H_0} u dz, \quad N = \int_{H_0-h}^{H_0} v dz. \quad (11)$$

[22] The parameters M and N are obtained from the velocity components integrated along the z axis from the sea bottom ($z = H_0 - h$) to the sea surface ($z = H_0$).

[23] When the right hand sides of equation (9) are neglected, the linear long-wave (LLW) equations are obtained as

$$\begin{aligned} \frac{\partial M}{\partial t} + gh \frac{\partial \eta}{\partial x} &= 0, \\ \frac{\partial N}{\partial t} + gh \frac{\partial \eta}{\partial y} &= 0. \end{aligned} \quad (12)$$

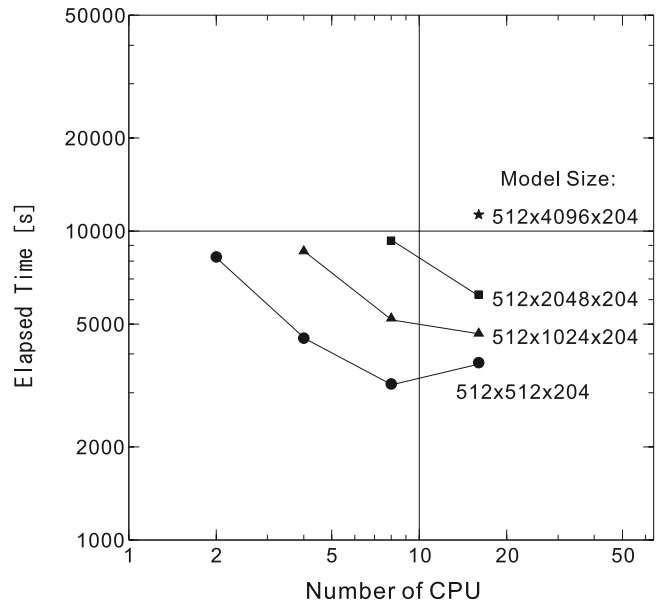


Figure 4. Parallel performance of the parallel 3-D Navier-Stokes simulation in terms of the elapsed time of the tsunami simulation as a function of CPU numbers and for different scales of the simulation model.

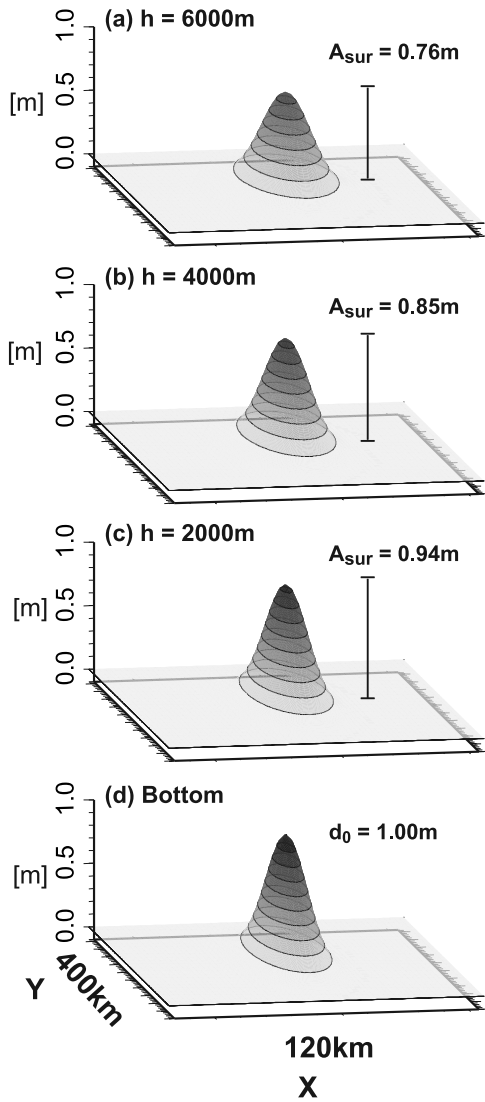


Figure 5. Elevation at the surface caused by vertical deformation at the bottom with a sea depth of (a) $h = 6000$ m, (b) 4000 m, and (c) 2000 m. Maximum height at the surface A_{sur} is also shown. (d) The source area at the bottom is characterized by $2a_x = 20$ km, $2a_y = 200$ km, and maximum elevation $d_0 = 1$ m.

[24] Many tsunami studies employ the LLW equations (equations (10) and (12)) to simulate tsunami propagation [e.g., Geist, 2002; Baba et al., 2006]. We numerically solve the LLW equations by the method often used in conventional studies [e.g., Satake, 1989]. The equation (12) cannot simulate dispersive tsunami in itself. However, it should be noted that there is a novel method to generate numerical dispersion using a coarse grid spacing in solving equation (12) instead of calculating rigorous dispersive tsunami equations [Shuto, 1991]. This study takes fine grid spacing to suppress the numerical dispersion in the simulation. We use the DSP equations (equations (9) and (10)) also for the comparisons in the later section. An implicit scheme is employed for solving the DSP equations [e.g., Shigihara and Fujima, 2007].

[25] There are some methods for implementing a tsunami source in the 2-D tsunami simulations. As the simplest one,

the initial tsunami distribution is assumed to be identical to the deformation at the bottom i.e., that $\eta(x, y, 0) = d(x, y)$ [e.g., Piatanesi and Lorito, 2007]. Another method is based on the continuity equation (10); the sea bottom deformation within the time step is added to the sea surface fluctuation for each time step in the simulation. Through this procedure, the source process time of the sea bottom deformation can be taken into account in the 2-D simulation [e.g., Fujii and Satake, 2008]. The third method employs the linear approximation theory to obtain the sea surface elevation caused by the sea bottom deformation [e.g., Kajiura, 1963]. The sea surface elevation can be used as the initial tsunami height distribution in the 2-D simulations [e.g., Tanioka and Seno, 2001].

[26] In the following section, we simulate the tsunami generation process due to the sea bottom deformation on the basis of the 3-D simulation, and compare the results with the above tsunami source implementation techniques.

3. Tsunami Generation and Propagation

3.1. Tsunami Generation

[27] We conduct 3-D simulation to investigate tsunami generation properties caused by the deformation of the sea bottom due to the earthquake. We suppose that the sea bottom deformation caused by the earthquake is given by a Gaussian function as follows:

$$d(x, y) = d_0 \exp\left\{-\frac{(x - x_0)^2}{a_x^2} - \frac{(y - y_0)^2}{a_y^2}\right\}, \quad (13)$$

where d_0 is the maximum height of the deformation, and $2a_x$ and $2a_y$ are the characteristic spatial lengths of the deformation area along the x and y axes, respectively. The simulation is conducted for different source models that are described by widths of $2a_x = 200, 100, 40,$ and 20 km, and a common length of $2a_y = 200$ km. A length of $2a_y = 200$ km roughly corresponds to the fault length associated with M8 earthquakes. One may take the view that the model with large $2a_x$ corresponds to a sea bottom deformation caused by a gently dipping seismic fault, and small values of $2a_x$ correspond to a steeply dipping seismic fault. We suppose that the bottom elevation starts at $t = 0$ and achieves a maximum height d_0 after a source process time t_s with constant velocity d_0/t_s .

[28] The models cover a region of 512 km by 512 km in the horizontal directions, and a constant sea depth of $h = 2000, 4000,$ and 6000 m, which has been discretized with a uniform mesh size of $\Delta x = \Delta y = 1$ km in the horizontal directions and $\Delta z = 100$ m in depth. The source process time is set to be $t_s = 20$ s. The NS simulation is conducted using a small time step of $\Delta t = 0.05$ s during the source process time and using a relatively large time step of $\Delta t = 0.5$ s after the source process time.

[29] Figure 5 shows the results of the surface height distribution at an elapsed time of $t = 20$ s for a common bottom deformation characterized by $2a_x = 20$ km, $2a_y = 200$ km and $d_0 = 1$ m for different sea depths of $h = 2000, 4000$ and 6000 m. The maximum height of the surface elevation for the shallow ($h = 2000$ m) model is 0.94 m, which is close to the corresponding bottom elevation d_0 . The shape of the height distribution at the surface is similar

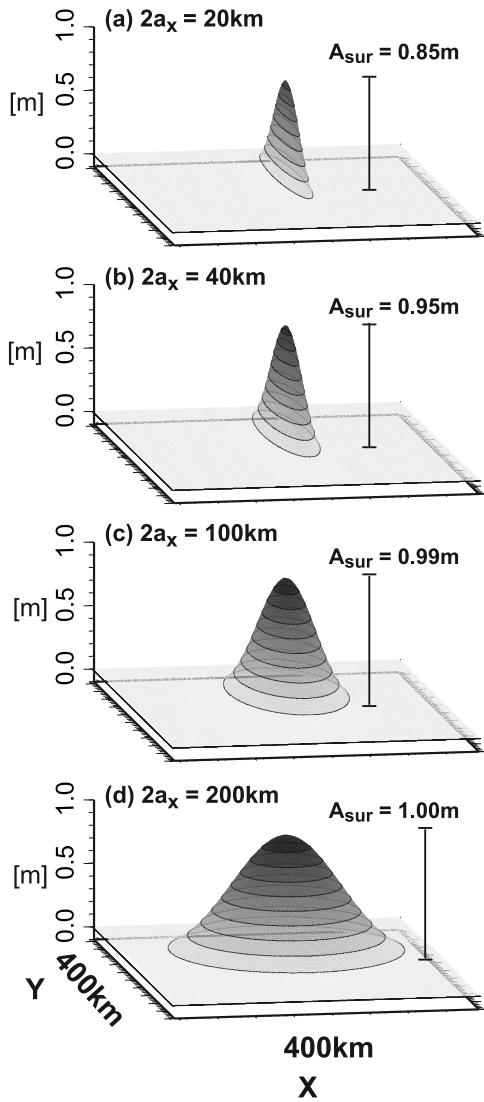


Figure 6. Elevation at the surface for a depth of $h = 4000$ m for different source widths at the sea bottom for (a) $2a_x = 20$ km, (b) $2a_x = 40$ km, (c) $2a_x = 100$ km, and (d) $2a_x = 200$ km. The source at the bottom is characterized by $2a_y = 200$ km and maximum elevation $d_0 = 1$ m.

to the bottom deformation. However, the surface height distribution is not identical to the bottom deformation, and the maximum height at the surface decreases with increasing sea depth. The maximum height for the deep ($h = 6000$ m) model is 0.76 m. Figure 5 illustrates broadening of the width of the tsunami and decreasing maximum amplitude at the surface; these effects become particularly apparent in deep sea. The broadening is the reflection of decreasing maximum height while retaining the total mass of water, since we are dealing with an incompressible fluid.

[30] We then examine the effect of source size on the tsunami generation by using different source sizes of $2a_x = 20, 40, 100, 200$ km and $a_y = 200$ km. The maximum deformation at the bottom is $d_0 = 1$ m, and we assume a common depth of $h = 4000$ m. Figure 6 shows the surface height distribution at an elapsed time of $t = 20$ s. The tsunami height decreases from 1.00 m to 0.85 m as the size

of the source decreases from 200 km to 20 km. This implies that a small area of bottom deformation caused by a small earthquake or by a steeply dipping fault cannot produce tsunami as high as the bottom deformation.

[31] We conduct a set of simulations using source models of $2a_x = 20, 40, 100,$ and 200 km, and depths of $h = 2, 4,$ and 6 km, and plot the maximum height at the surface as a function of source size $2a_x$ relative to the sea depth h (gray circle in Figure 7a). It shows a clear relation between the generation properties of tsunami for different depths and source sizes. A small source of width less than 10 times the sea depth ($2a_x < 10h$) cannot uplift the surface as high as the bottom deformation.

[32] In Figure 7a, we also plot the maximum height estimated by using the linear approximation theory [e.g., *Kajiura, 1963; Hammack, 1973*]. Since the elliptic sea bottom deformation is now supposed, we used the 2-D theory in the $(x-z)$ coordinates for the estimation. Furthermore, we plot the estimates based on the LLW equations with the continuity equation (gray square). The estimates of the linear approximation theory agree with our 3-D simu-

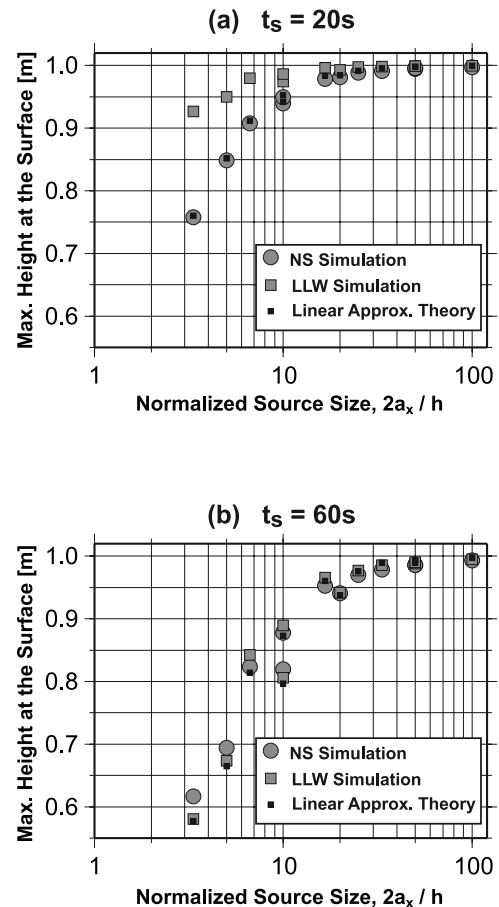


Figure 7. The maximum height at the surface as a function of source width relative to the depth $2a_x/h$, where $2a_x$ is the characteristic source width and h is the sea depth for the source process time of (a) 20 s and (b) 60 s. The height derived from the 3-D NS simulation, 2-D LLW simulation, and the linear approximation theory are plotted by gray circles, gray squares, and black squares, respectively.

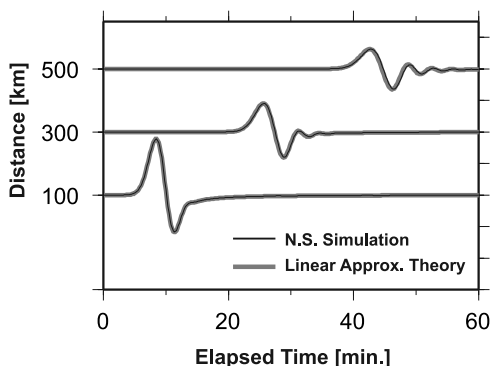


Figure 8. Comparison of tsunami waveform derived from 3-D NS simulation (black) and the linear approximation theory (gray) at travel distances of 100, 300, and 500 km for a sea depth of $h = 4000$ m and a circular source characterized by $a_x = a_y = 20$ km.

lation results, although the estimates of the LLW equations cannot reproduce the 3-D simulation results. It indicates that the linear approximation theory need to be employed for the estimation of a precise initial tsunami height distribution [e.g., Tanioka and Seno, 2001].

[33] We then conduct the tsunami generation simulations with relatively long source process time $t_s = 60$ s, and obtain Figure 7b. When the source process time is long, the maximum height becomes small for the same source size. When the source size is $2a_x/h = 3.3$, the maximum height is approximately 0.6 m in the case of the long source process

time of 60 s, while the maximum height is 0.75 m in the case of the short source process time of 20s. The long source process time decreases the maximum height in the tsunami generation process. When the source process time is 60 s, both the linear approximation theory and the LLW equations can reproduce the 3-D numerical simulation results (Figure 7b).

[34] Figures 7a and 7b indicate that the linear approximation theory is more suitable for the estimation of the initial tsunami height distribution than the method based on the LLW equations. In particular, when the source process time is short, the sea depth greatly contributes to the tsunami height distribution [e.g., Kajiura, 1963], which cannot be modeled by the LLW equations.

3.2. Tsunami Propagation

[35] We investigate the properties of tsunami propagation away from the source. Figure 8 shows the tsunami waveforms derived from the 3-D NS simulations (black curve) at the travel distances of 100, 300, and 500 km when the sea bottom deformation is given by $2a_x = 2a_y = 40$ km in a constant sea depth ($h = 4000$ m). At the longer travel distances (>300 km), the tsunami waveform show dispersion with long tails. In Figure 8, we also plot the solutions of the potential flow on the basis of the linear approximation theory [Takahashi, 1942] by gray curve to compare with our 3-D numerical simulation results. The results of our 3-D numerical simulation show excellent agreement with those by the linear approximation theory, which provides the evidence for the reliability of our simulation code.

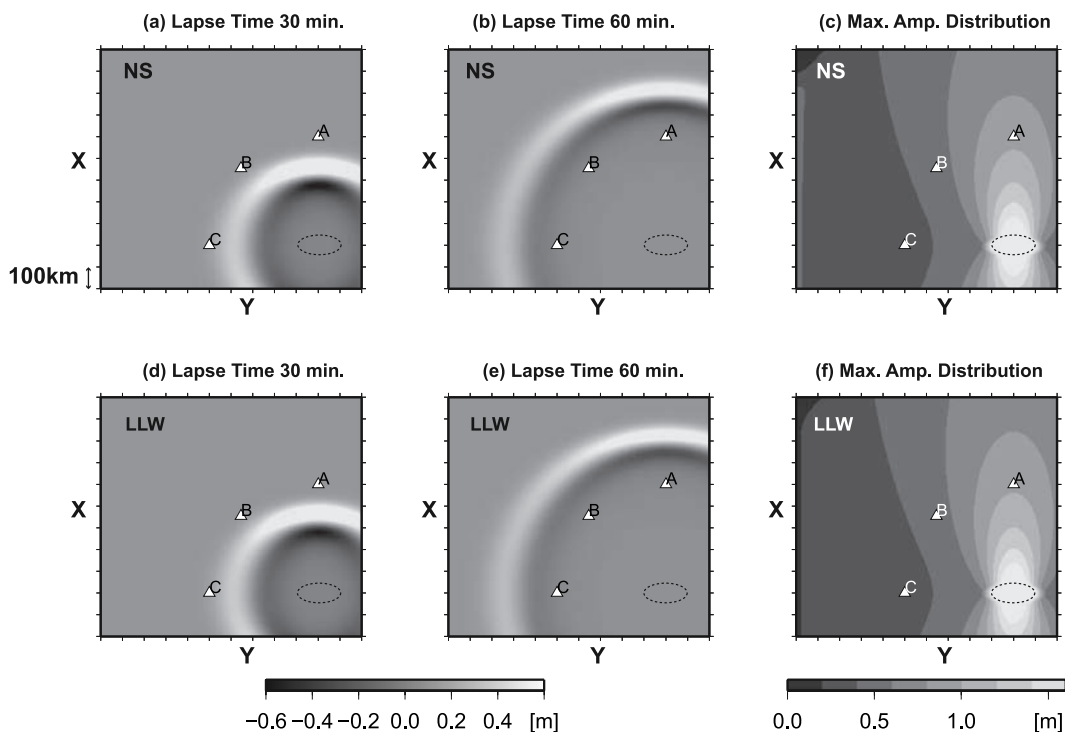


Figure 9. Snapshots of tsunami at elapsed times of (a) 30 min and (b) 60 min from the source origin time and (c) maximum height of the tsunami, calculated by the 3-D NS equations for a sea depth of $h = 4000$ m and a large source characterized by $2a_x = 100$ km and $2a_y = 200$ km. (d, e, f) Same as Figures 9a, 9b, and 9c but calculated from the 2-D LLW equations.

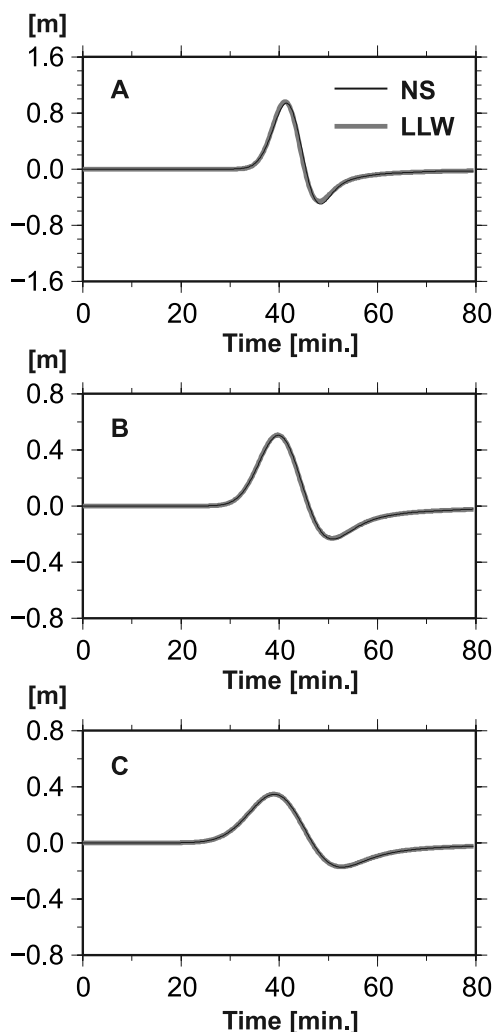


Figure 10. Tsunami records at stations A, B and C, calculated by using the 3-D NS equations (solid lines) and by the 2-D LLW equations (dashed lines). Locations of the three sources are shown in Figure 9.

[36] We then compare the simulation results of the 3-D NS equations and the LLW equations. Figures 9a and 9b show snapshots of tsunami propagation in a constant sea depth ($h = 4000$ m) at elapsed times of $t = 30$ and $t = 60$ min with a relatively large source area characterized by $2a_x = 100$ km, $2a_y = 200$ km, and $t_s = 60$ s. These snapshots are derived from the NS simulations. The snapshots show a clear pattern of tsunami radiation from an ellipsoidal source region (dashed circle); a large-amplitude tsunami propagates along the short axis of the source (the x axis) and a small-amplitude tsunami propagates along the long axis of the source (the y axis). Figure 9c shows the maximum amplitude distribution. Figure 10 shows the waveforms of tsunami recorded at stations A, B, C, located 500 km away from the center of the source. We confirmed a large-amplitude tsunami at station A and a small-amplitude tsunami at station C.

[37] The simulation results by the NS equations are compared with those derived by the LLW simulation. In the LLW simulations, we use the linear approximation theory [e.g., *Kajiura*, 1963] for the evaluation of the initial

tsunami height distribution and also take the finite source process time into account. The snapshots are shown in Figures 9d and 9e, and the maximum amplitude distribution is in Figure 9f. In general, good agreement between the two simulations is obtained in respect of the propagation properties. The waveforms of tsunami at stations A, B, and C (Figure 10) also show close agreement between the two simulation results. Those agreements (Figures 9 and 10) are reasonable since the LLW equations serve as good approximations to the NS equations when the wavelength is long enough compared with the sea depth.

[38] On the other hand, significant discrepancies between the 3-D NS and the 2-D LLW simulations arise when we use a narrow source with widths $2a_x = 30$ km and $2a_y = 200$ km (Figures 11a, 11b, 11c, 11d, and 11e). The width 30 km is smaller than 10 times the sea depth. Figures 11a and 11b show a strong dispersion of the tsunami propagation in the direction of the short source axis (the x axis), with a long tail of surface oscillations, which leads to significant attenuation in the leading tsunami as the wave propagates over long distances. Such dispersion characteristics do not arise in the LLW simulation; Figures 11d and 11e show impulsive leading waves spreading from the source with large amplitudes in the direction of the short source axis and small amplitudes in the direction of the long source axis.

[39] The maximum amplitude distributions resulting from the NS and LLW simulations are shown in Figures 11c and 11f. Those show clear discrepancies in the results of the two simulations. The LLW simulations result in larger tsunami amplitudes in the direction of the short source axis (the x axis), because the LLW simulation does not include any dispersion of the tsunami. However, the discrepancies in the tsunami between the two simulations are not obvious in the direction of the long source axis (the y axis), even at long distances.

[40] Figure 12 compares the tsunami records simulated on the basis of the NS and the LLW equations. The tsunami record at station A calculated from the NS simulation shows strong dispersion; the low-frequency leading wave is followed by high-frequency waves. This dispersion causes attenuation of the leading wave in its maximum amplitude. The maximum amplitude at station A for the NS simulation is approximately 60 % of the maximum amplitude for the LLW simulation, because the LLW simulation cannot simulate dispersive tsunami correctly. On the other hand, in the other directions, the dispersion of the tsunami is almost negligible, and thus the calculated tsunami records from LLW at stations B and C are almost identical to those calculated from the NS simulation.

4. Simulations of Two Intraplate Tsunami Events

[41] We apply 3-D NS simulations for two recent tsunami events which occurred in the subducting plates around Japan: the 2004 off-Kii Peninsula event (M 7.4) and the 2007 off-Kuril Island event (M 8.3).

4.1. Tsunami Simulation for the 2004 off-Kii Peninsula Earthquake

[42] At the Nankai Trough of southwestern Japan, where the Philippine Sea Plate is subducting underneath the Eurasian Plate (Figure 13), M8 earthquakes have repeatedly

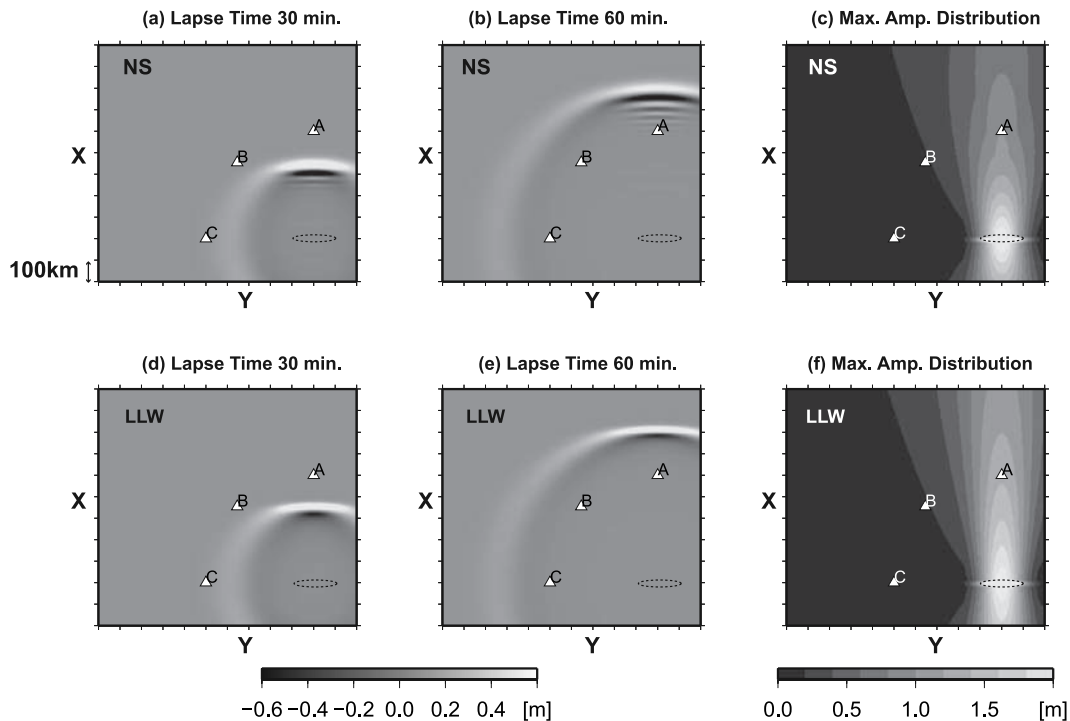


Figure 11. Snapshots of tsunami at elapsed times of (a) 30 min and (b) 60 min from the source origin time and (c) maximum height of the tsunami, calculated by the 3-D NS equations for a sea depth of $h = 4000$ m and a small source characterized by $2a_x = 30$ km and $2a_y = 200$ km. (d, e, f) Same as Figures 11a, 11b, and 11c but calculated from the 2-D LLW equations.

occurred along the plate interface with a recurrence interval in the order of 100 years. The previous events of the Tonankai (M 7.9) earthquake in 1944 and the Nankai (M 8.0) earthquake in 1946 caused serious tsunami damage along the Pacific coast of Japan.

[43] A large earthquake (Japan Meteorological Agency magnitude of M_{JMA} 7.4) occurred recently off Kii Peninsula on 5 September 2004. Unlike the Tonankai and Nankai earthquakes, this event was an intraplate event occurring in the outer rise of the subducting Philippine Sea Plate and the earthquake source was characterized by a thrust fault with a large dip angle (K. Yamanaka, unpublished data available at http://www.eri.u-tokyo.ac.jp/sanchu/Seismo_Note/2004/EIC153.html, 2004). This earthquake caused tsunami height less than 0.9m along the Japanese coast [e.g., *Matsumoto and Mikada*, 2005].

4.1.1. Simulation Model for the 2004 off–Kii Peninsula Event

[44] We simulate the tsunamis of the 2004 off–Kii Peninsula event on the basis of 3-D simulation. The area of the simulation model is 580 km by 896 km horizontally, extended to a depth of 10 km, which is discretized with grid size of 1 km in horizontal directions and 0.2 km vertically (Figure 13). Digital bathymetric data of J-EGG500, provided by the Japan Oceanographic Data Center, was employed in the simulation.

[45] The earthquake fault model for the 2004 Kii Peninsula event was derived from the analysis of far-field seismograms by K. Yamanaka (unpublished data available at http://www.eri.u-tokyo.ac.jp/sanchu/Seismo_Note/2004/EIC153.html, 2004). Referring to this model, we set param-

eters for a constant slip model on a flat fault plane. The top depth of the fault was 2 km and the fault sizes were 60 km and 32 km in the strike and dip directions, respectively. The focal parameters were given by dip = 40° , strike = 135° , rake = 120° , and the source process time was 30 s.

[46] The static deformation of the sea bottom caused by the earthquake was calculated from an analytical solution of the static deformation in elastic half-space [*Okada*, 1985]. The elastic parameters were taken as $V_p = 5.8$ km s^{-1} , $V_s = 3.2$ km s^{-1} , and $\rho = 2.6$ g cc^{-1} for our simulation, corresponding to the P and S -wave velocities of the upper crust of the Preliminary Reference Earth Model (PREM) [*Dziewonski and Anderson*, 1981]. The temporal change in the deformation of the sea bottom was introduced in the 3-D NS simulation through a vertical flow of water at the sea bottom (equation (5)) at a constant rate during the source process time.

4.1.2. Results of 3-D NS Simulations

[47] The results of tsunami simulation derived from the 3-D simulation are compared with an observed tsunami record. The Japan Agency for Marine–Earth Science and Technology Center (JAMSTEC) operates bottom pressure gauges offshore of Muroto at a depth of 2300 m (point M in Figure 13). The tsunami gauge measures the pressure at the sea bottom caused by tsunamis, and the tsunami records can be converted from the time history of the pressure gauge. Such an offshore tsunami gauge is suitable to examine tsunami generation and propagation, since the records are free from strong local site effects inside the bay or near the coast. We applied a low-pass filter with a cutoff period 90s in order to remove short-period noise.

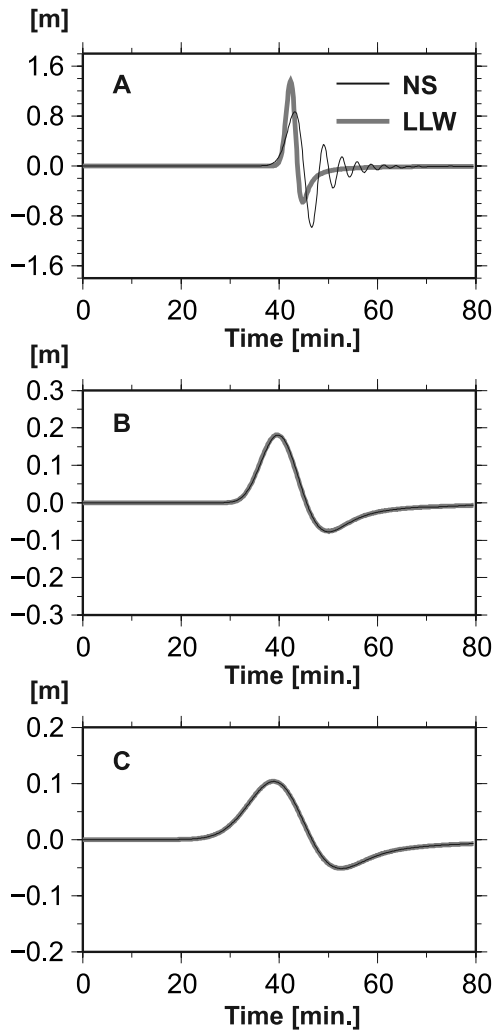


Figure 12. Same as Figure 10 but derived from a small source ($2a_x = 30$ km, $2a_y = 200$ km) model.

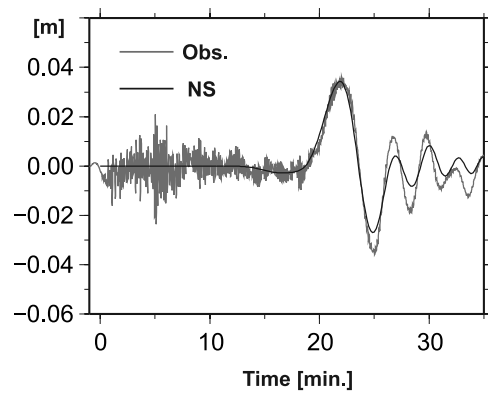


Figure 14. Tsunami record (gray curve) observed at station M in Figure 13 and tsunami records calculated from the 3-D NS simulations (solid curve).

Then, we approximated the tidal component by fitting a polynomial function and removed the tides from the records.

[48] The gray line in Figure 14 illustrates the observed tsunami at the offshore station M. At the beginning of the record (gray curve), high-frequency seismic waves arrive, and then large (>0.04 m) and long-period tsunami at dominant periods of approximately 5 min arrive at a time of around 18 min. After the leading tsunami, tsunami waves are oscillating for more than 20 min and form a long tail. Tsunami records simulated by the 3-D NS (solid curve) are plotted together in Figure 14. The magnitudes of the event was estimated to be $M_0 = 6.6 \times 10^{19}$ Nm (M_w 7.1) from the observed record. The results of 3-D NS equations were able to simulate the arrival time of the maximum amplitude and the features of the long tsunami tails.

4.1.3. Comparisons With Various Simulation Methods

[49] The results of the 3-D NS tsunami simulation are compared with those calculated by the LLW and DSP equations. All the simulations use the same bathymetry grid

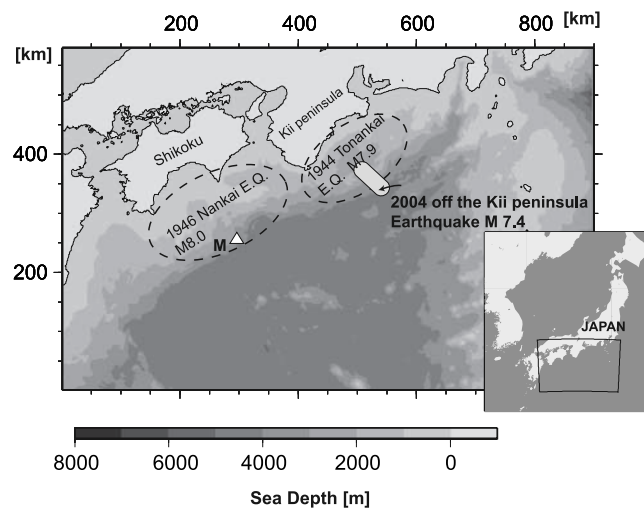


Figure 13. The area and bathymetry for the tsunami simulation of the 2004 M 7.4 off-Kii Peninsula earthquake (shaded area). Source areas of the 1944 Tonankai (M 7.9) and the 1946 Nankai (M 8.0) earthquakes are also shown by dashed curves. The location of an ocean bottom pressure gauge is shown by a triangle (M).

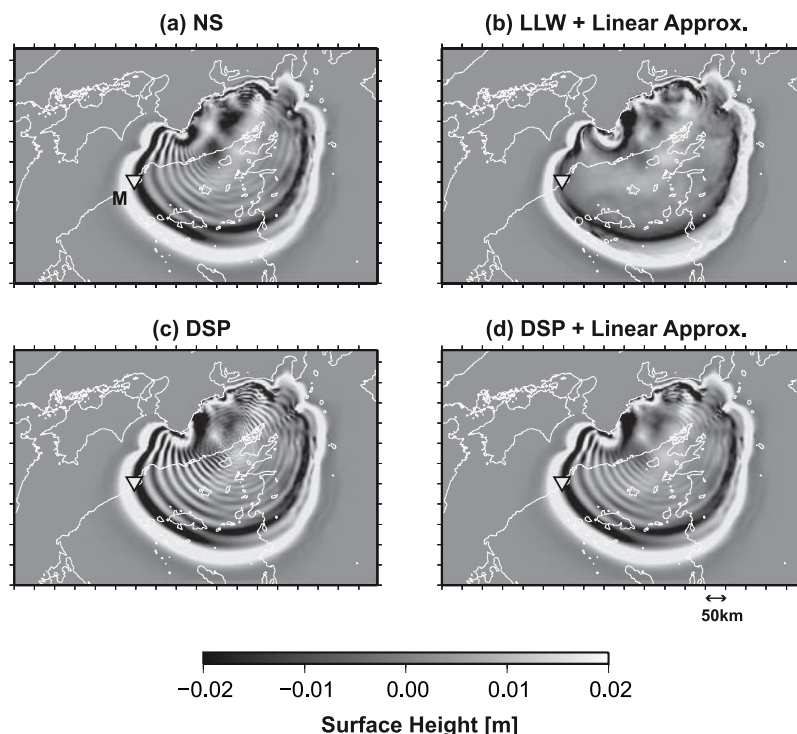


Figure 15. Surface height distribution for the 2004 off-Kii Peninsula event at an elapsed time $t = 24$ min from the earthquake origin time calculated by various methods, (a) the NS equations, (b) the LLW equations for the initial tsunami distribution estimated on the basis of the linear approximation theory, (c) the DSP equations for the initial tsunami distribution identical to the sea bottom deformation, and (d) the DSP equations for the initial tsunami distribution estimated on the basis of the linear approximation theory. A common source process time of 30 s is taken into account.

and the same fault model. The results of tsunami simulations are compared in Figure 15 as snapshots of tsunami propagation at an elapsed time of $t = 24$ min. In the LLW simulation (Figure 15b), we use linear approximation theory for evaluating initial tsunami distribution and also take the finite source process time is taken into account ($t_s = 30$ s). There is a significant difference between the NS and LLW simulations; the dispersion of tsunami propagation can be clearly seen from the NS simulation (Figure 15a), while the LLW simulation shows a simple impulsive shape in its leading wave (Figure 15b).

[50] Figures 15c and 15d are the results of the DSP equations; Figure 15c assume that initial tsunami distribution is identical to the sea bottom deformation, while Figure 15d uses the linear approximation theory to estimate the initial tsunami distribution. Both in Figures 15c and 15d, the finite source process time is taken into account ($t_s = 30$ s). In both results, clear dispersive tsunami is recognized. However, excessive dispersion appears when the linear approximation theory is not used in the estimation of the initial tsunami distribution (Figure 15c). On the other hand, when we use the linear approximation theory (Figure 15d), the simulation result is very similar to that of the NS simulation (Figure 15a). It is because the steep deformation, or short-scale fluctuations of the sea bottom deformation remains in the initial tsunami distribution in Figure 15c, while such short-scale fluctuations are removed by the deep

seawater in the tsunami generation process (Figures 15a and 15d).

[51] In Figure 16, we compare the tsunami waveforms synthesized by various methods. The results of 3-D NS equations and DSP equations are able to simulate the arrival time of the maximum amplitude and the features of the long-tail waves. On the other hand, as we see in the snapshots in Figure 15b, the 2-D LLW simulation shows an impulsive leading wave without a long tail. Also, the arrival time of the 2-D LLW simulation is about 1 min earlier than the observed record. The comparison indicates the importance of the modeling of the dispersion using proper tsunami equations.

4.2. Tsunami Simulation for the 2007 off-Kuril Islands Earthquake

[52] We conduct a 3-D simulation for another intraplate event occurring in the Pacific Plate off the Kuril Islands. The Kuril Islands form an island arc associated with the subducted Pacific Plate underneath the North American plate, and the Kuril trench is more than 8000 m deep (Figure 17). On 13 January 2007, a large M_{JMA} 8.1 earthquake occurred off the Kuril Islands. This earthquake was a normal fault event with a large dip angle (45°), occurring in the subducting plate beneath the Kuril trench. Considering the difficulty of tsunami simulation for the

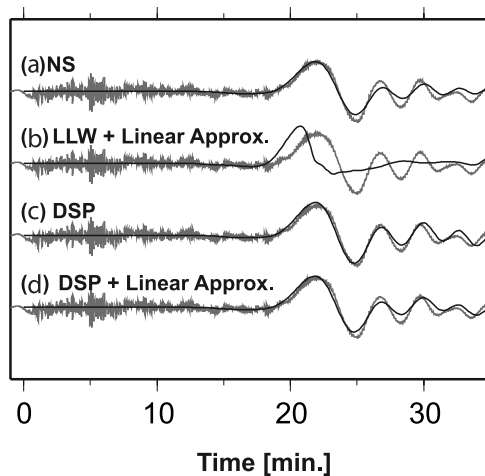


Figure 16. Comparisons of the tsunami waveforms synthesized by various methods, (a) the NS equations, (b) the LLW equations for the initial tsunami distribution estimated on the basis of the linear approximation theory, (c) the DSP equations for the initial tsunami distribution identical to the sea bottom deformation, and (d) the DSP equations for the initial tsunami distribution estimated on the basis of the linear approximation theory. A common source process time of 30 s is taken into account.

intraplate event based on conventional 2-D LLW simulations, we conduct a 3-D NS simulation for this event, and investigate the differences between the results of the two simulations.

4.2.1. Simulation Model for the 2007 Kuril Event

[53] The area of the simulation model was 1600 km by 2048 km horizontally, and extended to a depth of 22 km, which is discretized into $1600 \times 2048 \times 110$ grid points with a uniform mesh size of 1 km in the horizontal directions and 0.2 km in depth (Figure 17). Digital bathymetric data of ETOPO2 provided by the consortium of NOAA, NESDIS, and NGDC was employed in the simulation. The fault model for the Kuril Islands event in 2007 was derived from the analysis of tsunami waveforms by *Fujii and Satake* [2008]. The top depth of the fault was 7 km and the fault sizes were 240 km and 40 km in the strike and dip directions, respectively. The focal parameters were given by dip = 45° , strike = 215° , rake = -110° . The fault was divided into six subfaults and the slip on each subfault was estimated from the tsunami analysis. The source process time of 50 s was assumed in their estimation. We use the slip model of *Fujii and Satake* [2008] in the following simulation.

4.2.2. Simulation Results: Comparison With 2-D Linear Long-Wave Simulations

[54] The results of tsunami derived from the NS and LLW simulations are compared in Figure 18 using snapshots of tsunami propagation at an elapsed time of $t = 40$ min. There is a significant difference between the two results; the dispersion of tsunami propagation in the direction perpendicular to the fault strike (along the x axis) can be clearly seen from the NS simulation (Figure 18a). The wave train is

developed near the wavefront because of the dispersion in the deep sea. The dispersion of tsunami traveling in the deep sea results in long-wavelength leading tsunamis in the NS simulation. On the other hand, the LLW simulation shows a simple impulsive leading wave in this direction (Figure 18b).

[55] The strong dispersion in the NS simulation appears in the direction perpendicular to the fault strike, while the dispersion is weak in the direction along the fault strike. Such strong azimuthal dependence of tsunami propagation have been also seen in the snapshots of tsunami from an elliptical source in a constant sea depth model (Figure 11).

[56] The tsunami waveforms calculated by the two methods are compared in Figure 19. The simulated tsunami shows strong dispersion in the NS simulation and it forms a long wave train (Figure 19a). In contrast, the tsunami in the LLW simulation shows no dispersion and a sharp leading wave. The calculated tsunami waveforms were compared with the observed waveform off Kushiro, located about 1000 km from the source region (point K in Figure 17). The Japan Agency for Marine-Earth Science and Technology (JAMSTEC) operates bottom pressure gauges offshore of Kushiro at a depth of 2200 m. The gray line in Figure 19b illustrates the observed tsunami at the offshore station. At the beginning of the observed record at a time before 20 min, a large-amplitude high-frequency seismic wave arrives, and then large and long-period tsunami at periods of approximately 30 min arrive near a time of 60 min. Solid and dashed lines shown in Figure 19b for station K indicate the tsunami derived from the NS and LLW simulations, respectively. The tsunami waveforms calculated using the two simulations show no significant differences around the main part of the tsunami. This is

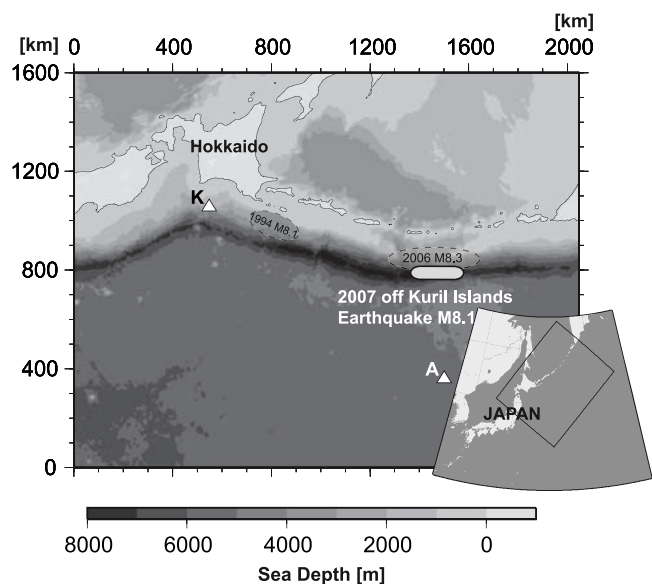


Figure 17. The area and bathymetry for the tsunami simulation of the 2007 M 8.1 off-Kuril Islands earthquake (shaded area). Source areas of the 1994 off-Kuril Islands (M 8.1) and the 2006 off-Kuril Islands (M 8.3) earthquakes are also shown by dashed curves. The location of an ocean bottom pressure gauge is shown by a triangle (K).

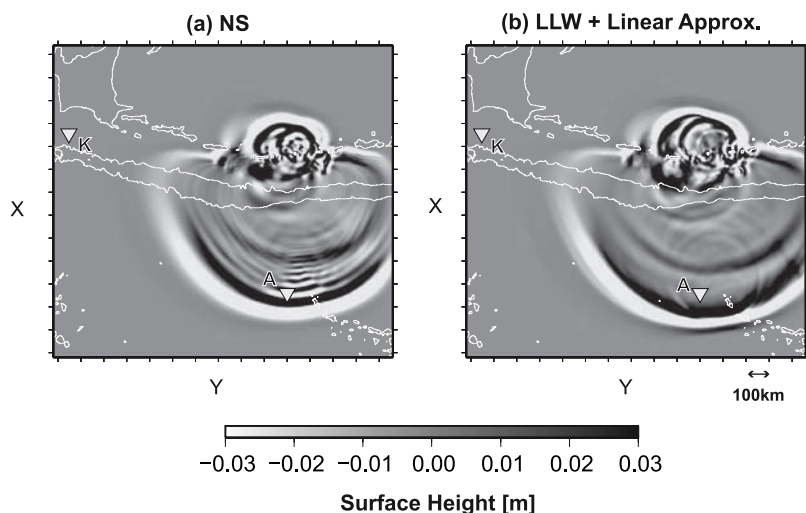


Figure 18. Surface height distribution for the 2007 off-Kuril Islands event at an elapsed time $t = 40$ min from the earthquake origin time calculated from the (a) NS and (b) LLW simulations.

mainly because there was negligible dispersion apparent in this direction.

5. Discussion

[57] The simulation results for both constant sea depth (section 3) and real bathymetry (section 4) indicate that significant differences arise between the simulation results of the 3-D NS and the 2-D LLW equations for small deformation area and for large dip angle earthquakes. The difference is mainly caused by the dispersion appearing in the tsunamis propagation. The dispersion, in general, depends on the propagation direction because the sea bottom deformation can be approximated as an elliptical distribution with a long axis in the fault strike direction and a short axis in the fault dip direction. Strong dispersion appears in the direction perpendicular to the fault strike where the large-amplitude tsunami is expected to arrive. We should take care in employing the 2-D LLW equations as approximations to the NS equations when the source is of small size; in particular, for tsunamis propagating in a direction perpendicular to the fault strike.

[58] In section 4, we confirmed that 2-D tsunami simulation can reproduce the results of the 3-D simulation if we take dispersion effect into account and use the initial tsunami distribution estimated carefully on the basis of the linear approximation theory (Figure 15d). The computational time in the 2-D simulation is approximately 30 min on a standard single-processor computer, while the 3-D simulation took approximately 6 h on parallel computers for the 2004 Kii Peninsula event. In view of computational time, the 2-D simulation is much more efficient than the 3-D simulation. However, steadily increasing computer power and parallel computing techniques using large number of processors will enable us to conduct large-scale 3-D simulations in far less time. The effects of the deep sea on the initial tsunami height distribution [e.g., *Kajiura, 1963*] and the tsunami dispersion during the propagation across deep sea

[e.g., *Carrier, 1971*] have been well known. This study has shown that the 3-D numerical simulation can nicely unify those tsunami generation and propagation simulations with realistic bathymetry by using a current powerful computer.

[59] Some studies insist on the importance of a heterogeneous subsurface structure for tsunami generation, such as soft sediments [e.g., *Fukao, 1979*]. The sea bottom deformation caused by an earthquake in such 3-D heterogeneous structure can be numerically simulated by using a 3-D seismic wave propagation modeling [e.g., *Wald and Graves,*

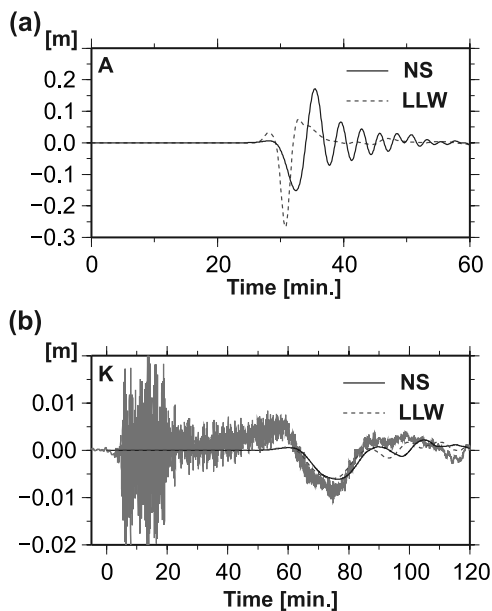


Figure 19. (a) Tsunami waveforms calculated from the simulations using the NS equations (solid curve) and the LLW equations (dashed curve), at station A in Figure 17. (b) A tsunami waveform (gray curve) observed at station K shown in Figure 17. Tsunami waveforms calculated from the simulation using the NS equations (solid curve) and the LLW equations (dashed curve) are plotted together.

2001]. For linking the spatial and temporal variation of the sea bottom deformation to tsunami generation and propagation, the 3-D tsunami simulation is suitable since it explicitly calculates the vertical flow from the sea bottom.

6. Conclusions

[60] A parallel FDM program based on the 3-D NS equations has been developed for simulating tsunami generation caused by sea bottom deformation and the consequent offshore tsunami propagation over more than 1000 km. By employing this method on current powerful computers, we have simulated tsunami generation and propagation with real bathymetry, and have confirmed that the simulated records agreed closely with tsunami observations from two intraplate earthquake.

[61] The results from the 3-D NS simulations show that a sea bottom deformation confined to a small area cannot uplift the sea surface as high as the sea bottom deformation. We have found a significant difference between the sea bottom deformation and the sea surface uplift when the source width $2a_x$ is less than 10 times the sea depth h ($2a_x \leq 10h$) for a source process time of 20 s. The sea surface distribution can be reproduced by the linear approximation theory. The surface distribution estimated by the linear approximation theory can work well as an initial tsunami distribution in the 2-D simulations. Furthermore, dispersion of tsunami appears clearly when the tsunami propagates over long distances when the source is of small size. The dispersion shows directional dependence; dispersion is more apparent in a direction perpendicular to the fault strike.

[62] In order to demonstrate the effectiveness of the 3-D tsunami simulations, we have simulated two recent tsunami events occurring within subducting plates around Japan; the 2004 off-Kii Peninsula (M_{JMA} 7.4) and the 2007 off-Kuril Islands (M_{JMA} 8.1) earthquakes. The 3-D tsunami simulation successfully simulated the offshore tsunamis and we obtained close agreement between the observations and the calculations for both events. In particular, for the 2004 off-Kii Peninsula event, although the 2-D LLW simulation cannot simulate important characteristics in the record such as the arrival time of the peak amplitude and the dispersive tsunamis, the 3-D simulation was well able to model those characteristics.

[63] **Acknowledgments.** We used records from the bottom pressure gauge operated by the Japan Agency for Marine-Earth Science and Technology (JAMSTEC). This study was supported by a grant-in-aid from the Core Research for Evolutional Science and Technology (CREST), the Japan Science and Technology Agency. We thank the EIC for supporting our use of CPU time. We thank Y. Tanioka, Y. Namegaya, and H. Matsumoto for discussion and fruitful advice on this study. Careful reading of the manuscript and constructive comments by anonymous reviewers, associate editor and editor P. Taylor were very valuable for revision of the paper.

References

Baba, T., P. R. Cummins, and T. Hori (2006), High precision slip distribution of the 1944 Tonankai earthquake inferred from tsunami waveforms: Possible slip on a splay fault, *Tectonophysics*, *426*, 119–134, doi:10.1016/j.tecto.2006.02.015.

- Carrier, G. F. (1971), The dynamics of tsunamis, in *Mathematical Problems in the Geophysical Sciences: I. Geophysical Fluid Dynamics*, edited by W. H. Reid, pp. 157–187, Am. Math. Soc., Providence, R. I.
- Cerjan, C., D. Kosloff, R. Kosloff, and M. Reshef (1985), A nonreflecting boundary condition for discrete acoustic and elastic wave equations, *Geophysics*, *50*, 705–708, doi:10.1190/1.1441945.
- Dziewonski, A. M., and D. L. Anderson (1981), Preliminary reference Earth model, *Phys. Earth Planet. Inter.*, *25*, 297–356, doi:10.1016/0031-9201(81)90046-7.
- Fujii, Y., and K. Satake (2007), Tsunami source of the 2004 Sumatra-Andaman earthquake inferred from tide gauge and satellite data, *Bull. Seismol. Soc. Am.*, *97*, 192–207, doi:10.1785/0120050613.
- Fujii, Y., and K. Satake (2008), Tsunami source of the November 2006 and January 2007 great Kuril earthquakes, *Bull. Seismol. Soc. Am.*, *98*, 1559–1571, doi:10.1785/0120070221.
- Fukao, Y. (1979), Tsunami earthquakes and subduction processes near deep-sea trenches, *J. Geophys. Res.*, *84*, 2303–2314, doi:10.1029/JB084iB05p02303.
- Geist, E. L. (2002), Complex earthquake rupture and local tsunamis, *J. Geophys. Res.*, *107*(B5), 2086, doi:10.1029/2000JB000139.
- Goto, C. (1984), Equations of nonlinear dispersive long waves for a large Ursell number (in Japanese with English abstract), *J. Hydraul. Coastal Environ. Eng.*, *351*, 193–201.
- Hammack, J. (1973), A note on tsunamis: Their generation and propagation in an ocean of uniform depth, *J. Fluid Mech.*, *60*, 769–799, doi:10.1017/S0022112073000479.
- Heinrich, P., A. Piatanesi, and H. Hébert (2001), Numerical modeling of tsunami generation and propagation from submarine slumps: The 1998 Papua New Guinea event, *Geophys. J. Int.*, *145*, 97–111, doi:10.1111/j.1365-246X.2001.00336.x.
- Hirt, C. W., B. D. Nichols, and N. C. Romero (1975), SOLA—A numerical solution algorithm for transient fluid flows, *Rep. LA-5852*, Los Alamos National Laboratory, Los Alamos, N. M.
- Kajiura, K. (1963), The leading wave of a tsunami, *Bull. Earthquake Res. Inst. Univ. Tokyo*, *41*, 545–571.
- Kervella, Y., D. Dutykh, and F. Dias (2007), Comparison between three-dimensional linear and nonlinear tsunami generation models, *Theor. Comput. Fluid Dyn.*, *21*, 245–269, doi:10.1007/s00162-007-0047-0.
- Mader, C. L. (2004), *Numerical Modeling of Water Waves*, CRC Press, Boca Raton, N. Y.
- Matsumoto, H., and H. Mikada (2005), Fault geometry of the 2004 off the Kii Peninsula earthquake inferred from offshore pressure waveforms, *Earth Planets Space*, *57*, 161–166.
- Ohmachi, T., H. Tsukiyama, and H. Matsumoto (2001), Simulation of tsunami induced by dynamic displacement of seabed due to seismic faulting, *Bull. Seismol. Soc. Am.*, *91*, 1898–1909, doi:10.1785/0120000074.
- Okada, Y. (1985), Surface deformation due to shear and tensile faults in a half space, *Bull. Seismol. Soc. Am.*, *75*, 1135–1154.
- Piatanesi, A., and S. Lorito (2007), Rupture process of the 2004 Sumatra-Andaman Earthquake from Tsunami waveform inversion, *Bull. Seismol. Soc. Am.*, *97*, 223–231, doi:10.1785/0120050627.
- Satake, K. (1989), Inversion of tsunami waveforms for the estimation of heterogeneous fault motion of large submarine earthquakes: The 1968 Tokachi-oki and 1983 Japan Sea earthquakes, *J. Geophys. Res.*, *94*, 5627–5636, doi:10.1029/JB094iB05p05627.
- Shigihara, Y., and K. Fujima (2007), Adequate numerical scheme for dispersive wave theory for tsunami simulation and development of new numerical algorithm (in Japanese with English abstract), *J. Jpn. Soc. Civ. Eng.*, *63*, 51–66.
- Shuto, N. (1991), Numerical simulation of tsunamis—Its present and near future, *Nat. Hazards*, *4*, 171–191, doi:10.1007/BF00162786.
- Snider, R. (2001), *A Guide Tour of Mathematical Method*, Cambridge Univ. Press, Cambridge, U. K.
- Stoker, J. J. (1958), *Water Waves: The Mathematical Theory with Applications*, John Wiley, Hoboken, N. J.
- Stoneley, R. (1964), The propagation of tsunamis, *Geophys. J. R. Astron. Soc.*, *8*, 64–81.
- Takahashi, R. (1942), On seismic sea waves caused by deformations of the sea bottom (in Japanese with English abstract), *Bull. Earthquake Res. Inst. Univ. Tokyo*, *41*, 545–571.
- Tanioka, Y., and T. Seno (2001), Sediment effect on tsunami generation of the 1896 Sanriku tsunami earthquake, *Geophys. Res. Lett.*, *28*, 3389–3392, doi:10.1029/2001GL013149.
- Wald, D. J., and R. W. Graves (2001), Resolution analysis of finite source inversion using one- and three-dimensional Green's functions 2. Combin-

- ing seismic and geodetic data, *J. Geophys. Res.*, *106*, 8767–8788, doi:10.1029/2000JB900435.
- Ward, S. N. (2001), Landslide tsunami, *J. Geophys. Res.*, *106*, 11,201–11,215, doi:10.1029/2000JB900450.
- Yoon, S. B. (2002), Propagation of distant tsunamis over slowly varying topography, *J. Geophys. Res.*, *107*(C10), 3140, doi:10.1029/2001JC000791.

T. Furumura and T. Saito (corresponding author), Earthquake Research Institute, University of Tokyo, 1-1-1 Yayoi, Bunkyo-ku, 113-0032, Tokyo, Tokyo, Japan. (saito-ta@eri.u-tokyo.ac.jp)